PCCP

PAPER

View Article Online
View Journal | View Issue

Cite this: *Phys. Chem. Chem. Phys.*, 2017, **19**, 9478

Phonon bottleneck and long-lived excited states in π-conjugated pyrene hoop†

Ricardo Franklin-Mergarejo,[a] Tammie Nelson,[b] Sergei Tretiak*[b] and Sebastian Fernandez-Alberti*[a]

Received 5th January 2017,
Accepted 13th March 2017

DOI: 10.1039/c7cp00094d

rsc.li/pccp

In the last decade, recent synthetic advances have launched carbon-based π-conjugated hoops to the forefront of theoretical and experimental investigation not only for their potential use as bottom-up templates for carbon nanotube (CNT) growth, but also for the interesting excitonic effects arising from the cyclic geometry, unique π-system orientation, and unusual electronic interactions and couplings. In particular, cyclic materials based on pyrene, a common component in organic electronics, are popular candidates for the future design of π-conjugated nanorings for optoelectronic applications. Understanding the photophysical response in cyclic oligopyrenes can be achieved using non-adiabatic excited state molecular dynamics (NA-ESMD). Through NA-ESMD modeling, we reveal details of the nonradiative relaxation processes in the circular pyrene tetramer [4]cyclo-2,7-pyrenylene ([4]CPY) where we find that the strong non-adiabatic coupling combined with the dense manifold of excited states creates an internal conversion mechanism dominated by ultrafast sequential quantum transitions. However, we observe two long-lived electronic excited states that introduce a phonon bottleneck in the electronic relaxation process. In fact, the timescale for the electronic relaxation is almost exclusively dominated by the lifetimes of the long-lived states. We find that the states associated with the phonon bottleneck are separated from lower energy states by large energy gaps and are characterized by localization on a single pyrene unit resulting in a spatial mismatch with strongly delocalized neighboring states.

1 Introduction

Aromatic belt compounds, best described as hoop-shaped π-conjugated molecules, have captured the imagination of chemists and physicists alike due to their uniquely oriented π orbitals and the synthetic challenges involved in their preparation. The stability of various nanobelts and rings has been the subject of theoretical investigations[1–5] beginning as early as 1954.[6] Over the past decade, the development of several creative synthetic methods[2,7–12] has greatly accelerated the preparation and characterization of this class of compounds.

One of the primary motivations behind this enormous effort is the possibility of using carbon-based hoops in the bottom-up synthesis of carbon nanotubes (CNTs) with controlled chirality and diameter.[4,9,10,13,14] In addition, conjugated hoops have also become a popular test bed for studying molecular strain and intermolecular π–π interactions in curved systems.[5,7,9] Molecular strain in hoops can cause interesting photophysical properties due to the unconventional topology of the π system with orbitals situated parallel to the molecular plane rather than perpendicular. For example, it has been demonstrated that the absorption and emission properties could be tuned by controlling the torsion on a ring.[15] In paraphenylenes, differences in excitonic effects between linear and cyclic geometries gives rise to distinctive optical properties. In the cyclic orientation, the electron–hole pair experiences enhanced Coulomb interactions, similar to the confinement enhanced Coulomb interaction seen in semiconductor nanocrystals and quantum dots, an effect contributing to the unexpected increase of the optical absorption gap as a function of molecular size in cycloparaphenylenes (CPPs)[16] and resulting in slower nonradiative loss in other nanomaterials.[17] CPPs have also been found to be excellent fluorophores exhibiting a fluorescence quantum yield greater than 50% and becoming as large as 89%.[18] This phenomena was later attributed to the strong non-adiabatic coupling in CPPs which induces self trapping of the lowest excitonic state. The ultrafast formation of spatially localized excitations in large hoops ([>8]CPP) significantly alters optical selection rules making the Condon approximation invalid.[19]

The synthesis of CPPs often involves the use of biphenyl building blocks.[20] Other aromatic compounds, such as acenes and pyrene, have been incorporated in ring structures as well.[21,22]

[a] *Universidad Nacional de Quilmes/CONICET, Roque Saenz Peña 352, B1876BXD, Bernal, Argentina. E-mail: sfalberti@gmail.com*
[b] *Theoretical Division, Los Alamos National Laboratory, Los Alamos, New Mexico 87545, USA. E-mail: serg@lanl.gov*

† Electronic supplementary information (ESI) available: Contributions of excited states to the calculated absorption spectrum. See DOI: 10.1039/c7cp00094d

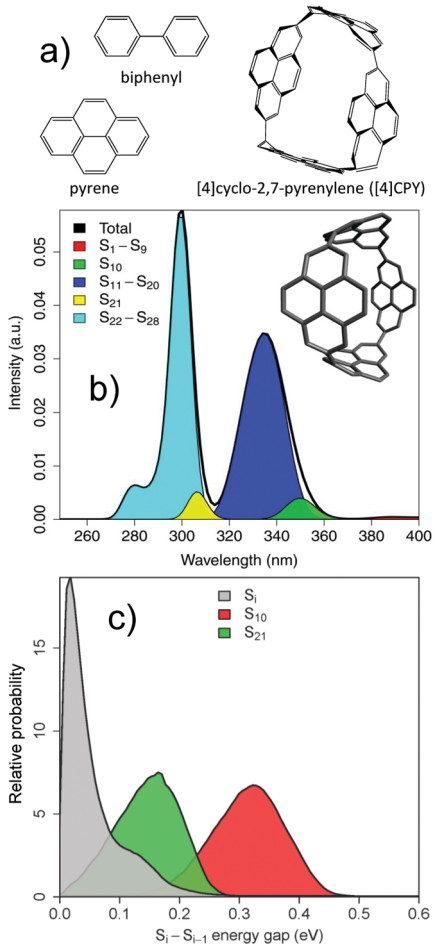

Fig. 1 (a) Chemical structures of biphenyl and pyrene and the cyclic pyrene tetramer [4]cyclo-2,7-pyrenylene formed by joining 4 pyrene units in a ring, denoted as [4]CPY. (b) Simulated absorption spectrum of [4]CPY where the contributions of different electronic states is highlighted. Absorption profiles were obtained using an effective Gaussian full width at half maximum of 0.01 eV. (c) Distribution of energy gaps between the current state and the state directly below in energy at the moment of electronic transition for S_{21}, S_{10}, and all other states S_i.

In particular, pyrene (see Fig. 1(a)), named for the Greek "fire", was first reported by Laurent in 1837 after discovering the compound in the residue of the destructive distillation of tar.[23] It has since become one of the omnipresent chromophores of material science appearing in several technological applications.[24] Its unique photophysical properties,[25] including concentration dependent excimer formation, long-lived excited states, high fluorescence quantum yields, and distinct emission bands sensitive to the microenvironment,[26] have been exploited for use in molecular sensors and probes.[27–33] Only recently, Itami and coworkers synthesized the first nanoring containing pyrene along with phenylene units.[21] That was quickly followed by the preparation of a cyclic pyrene tetramer denoted as [4]CPY, Fig. 1(a), containing only pyrene units.[22]

Thus, there has been an increased interest in the use of conjugated cycles and pyrene-based materials for optoelectronic applications.[34,35] Understanding the photophysical response in cyclic oligopyrenes such as optical properties, excited state dynamics, and nonradiative relaxation, is significant for the formulation of structure–property relationships and the synthetic design of π-conjugated nanorings for various technologies. Here, we have used non-adiabatic excited state molecular dynamics (NA-ESMD) simulations, to characterize the non-radiative relaxation mechanism in the cyclic pyrene tetramer, [4]cyclo-2,7-pyrenylene ([4]CPY), depicted in Fig. 1(a). Following photo-excitation, the presence of long-lived excited states creates a bottleneck in the sequential relaxation process. However, we find that the redistribution of excitation energy induces changes in exciton localization that allows the sequential mechanism to be overcome in favor of fast electronic relaxation.

The paper is organized as follows. Computational methods and details of the NA-ESMD simulations are described in Section 2. The results of the electronic relaxation dynamics and analysis of the time dependent electronic transition density localization are presented and discussed in Section 3. Finally, our findings and conclusions are summarized in Section 4.

2 Computational methods

2.1 NA-ESMD overview

The non-adiabatic excited state molecular dynamics (NA-ESMD) framework[36–41] uses the fewest switches surface hopping (FSSH) algorithm[42] to efficiently model the nonradiative relaxation through many coupled electronic excited states in large molecular systems. The nuclei are treated classically *via* constant-temperature Langevin dynamics[43,44] where forces are derived from a single adiabatic excited state potential energy surface (PES) and transitions among coupled excited state are computed based on non-adiabatic couplings. Meanwhile, "on-the-fly" analytical calculations of excited state energies, gradients, and non-adiabatic couplings[36,45–49] provide a quantum mechanical description of the electrons. The Collective Electronic Oscillator (CEO) approach[50,51] is used to compute excited states at the configuration interaction singles (CIS) level of theory. The CEO approach is based on the equation of motion[52] for the single-electron density-matrix[53] and has been implemented here with the semiempirical Hamiltonian models[54] to decrease the numerical demand associated with treating large molecular systems.

Within the CEO approach, the CIS eigenstates, written in the atomic orbital (AO) basis, are frequently denoted as transition density matrices (or electronic normal modes) and can be formally written[50,51] as

$$(\rho^{0\alpha})_{nm} = \langle \phi_\alpha(r;\mathbf{R}(t))|c_m^+ c_n|\phi_0(r;\mathbf{R}(t))\rangle \quad (1)$$

where the CIS adiabatic ground and excited state wave functions are represented by $\phi_0(r;\mathbf{R}(t))$ and $\phi_\alpha(r;\mathbf{R}(t))$, respectively. n and m are indices referring to the AO basis functions and c_m^+ and c_n are creation and annihilation operators such that the diagonal elements $(\rho^{0\alpha})_{nn}$ represent the changes in the distribution of electronic density caused by the light-induced excitation from the ground state S_0 to an excited electronic state S_α.[55]

The usual normalization condition $\sum_{n,m} \left(\rho^{0\alpha}\right)_{nm}{}^2 = 1$ holds for the CIS approximation.[45]

The time dependent (de)localization of the electronic transition density can be followed during NA-ESMD simulations using the participation number (PN) given by

$$\mathrm{PN} = \left[\sum_{X} \left(\left(\rho^{0\alpha}\right)_{X\text{-unit}}{}^2\right)^2\right]^{-1} \quad (2)$$

where $\left(\rho^{0\alpha}\right)_{X\text{-unit}}{}^2 = \sum_{n_A m_A} \left(\rho^{0\alpha}\right)_{n_A m_A}{}^2$ is the fraction of electronic transition density contained within unit X. Here, $(\rho^{0\alpha})_{nm}$ are the transition density matrix elements calculated within the CEO formalism[50,51] in the atomic orbital basis such that index A counts each atom on unit X. The participation number is defined taking each pyrene chromophore as a unit giving $1 \leq \mathrm{PN} \leq 4$. For a specific electronic state, this quantity measures the spatial delocalization of the excitonic wavefunction.[56] Due to the symmetry of the [4]CPY system, the four pyrene units can be considered indistinguishable among the swarm of individual trajectories. Therefore, the value of PN = 1 corresponds to localization of the electronic transition density within a single pyrene unit, no matter which of the four units comprising the nanohoop, and PN = 4 corresponds to delocalization over the entire ring.

2.2 Simulation details

The pyrene nanoring [4]CPY is composed of four pyrene monomers whose chemical structures are shown in Fig. 1(a). The photoinduced dynamics of [4]CPY has been modeled at room temperature (300 K). All calculations are performed using the semiempirical AM1 Hamiltonian.[54] We start by propagating ground state (GS) dynamics for 1 ns using a Langevin thermostat with a friction coefficient of 20 ps^{-1} to maintain thermal equilibration (300 K). Snapshots of 496 nuclear positions and momenta were sampled at 2 ps intervals from the GS trajectory to serve as initial conditions for the NA-ESMD simulations. Each initial configuration was instantaneously promoted to an initial excited state selected according to a Gaussian shaped Franck–Condon window[57] centered at 300 nm with a full width at half maximum (FWHM) of 100 fs. The NA-ESMD trajectories were then propagated for 500 fs with a classical timestep of Δt = 0.1 fs and quantum timestep of δt = 0.025 fs at 300 K using a friction coefficient of 20 ps^{-1}. Our FSSH non-adiabatic dynamics modeling includes corrections for decoherence[40] and trivial crossings.[38,39] Parameters and methodology of such NA-ESMD simulations have been extensively discussed elsewhere.[36–41] 30 singlet electronic excited states have been included in the dynamics and we label them using the common notation S_n, n = 1,...,30. The main contribution to the peak at low wavelength of the spectra (λ_{max} = 300 nm) corresponds to S_{25}, while contributions of upper states decrease significantly.

3 Results and discussion

3.1 Ground state and optical absorption

The ground state conformational sampling at T = 300 K reveals that the pyrene monomers in [4]CPY are torsionally distorted having alternating signs (±) of the interchromophore dihedral angles with an average torsion of 19.0° ± 10.5°. This relatively high level of molecular planarity suggests non-disrupted π-conjugation and a large delocalization of the electronic wave function. The computed absorption spectrum of [4]CPY, shown in Fig. 1(b), was obtained by collecting vertical transitions calculated from the equilibrated ensemble of GS snapshots. The maximum calculated absorption appears at λ_{max} = 300 nm, selected as the excitation wavelength for the NA-ESMD simulation. This is in good agreement with previously reported experimental UV/vis spectra[22] measured in $CHCl_3$ which places the maximum absorption coefficient at λ_{max} = 311 nm and exhibits a shoulder at lower energies that can be attributed to lower intensity absorption bands. Computed spectra also exhibit lower intensity absorption bands at wavelengths above λ_{max} extending to 400 nm, consistent with the measured spectra. However, in the absence of high-resolution experimental UV/vis spectra, precise identification of electronic states is not feasible.

Experimental measurements, however, were not able to determine which transitions give rise to the λ_{max} peak. According to our simulated spectrum, the contributions of states, as shown in Fig. 1(b), reveal five distinct bands. Each absorption band is associated with several states of the same electronic origin appearing as a quantum superposition of the parent monomer states. In addition, we observe electronic states delocalized across different units. Disorder effects introduce significant mixture in the dense excited state manifold in our conformational sampling. The ranges of states are assigned based on the contributions of all individual states to the computed absorption spectrum presented in Fig. S1 of ESI.† S_{22}–S_{28} are responsible for the λ_{max} peak. S_{21} is somewhat displaced from λ_{max} and, interestingly, a large energy gap separates S_{21} from the third band composed of S_{11}–S_{20}. Following this band, another band associated with S_{10} is separated from the final band S_1–S_9. The two large energy gaps following S_{21} and S_{10} imply a potential phonon bottleneck in the relaxation of electronic excitation energy across the state manifold.

3.2 Electronic relaxation dynamics

First, in order to rationalize the effects of density of excited states on nonradiative relaxation, the distribution of energy gaps during dynamics between S_{21}–S_{20}, S_{10}–S_9, and for all other states S_i–S_{i-1} ($i \neq 21, 10$) has been analyzed at the moment of transition to the lower energy state. The non-adiabatic coupling is inversely related to the energy gap, so that as the separation increases, it becomes less probable for the system to transition to lower lying states. The energy gaps are shown in Fig. 1(c) where the average gap between S_i and S_{i-1} is 0.04 eV. In contrast, the average difference in energy between S_{21} and S_{20} is considerably larger at 0.15 eV and is the largest between S_{10} and S_9 at 0.32 eV. These large energy gaps suggest that S_{21} and S_{10} could behave as long-lived states. Neither S_{21} nor S_{10} experience trivial unavoided crossings with energetically neighboring states in more than 10% of the NA-ESMD trajectories, therefore, a potential reordering in state energies does not significantly affect our results.

After the initial excitation of [4]CPY at λ_{max} = 300 nm, the internal conversion to the lowest energy S_1 state has been followed by tracking the electronic state populations (calculated as the fraction of trajectories in each state). The evolution of state populations is shown in Fig. 2(a). Due to thermal fluctuations generating a variety of molecular conformations, the initial excitation corresponds to the range of states S_{22}–S_{25}. The rise of the S_1 population (final state) is preceded by the population and subsequent depletion of S_{21} and S_{10} which, as expected, behave as distinct long-lived intermediates within the context of the ultrafast energy relaxation. Indeed, S_{10} retains the majority of the population density for almost 190 fs before relaxation to S_1 dominates.

Time scales for the relevant states S_{21}, S_{10}, and S_1 were obtained by fitting the population curves in Fig. 2(a) with exponential decay and growth functions of the form $f(t) = A\exp(-t/\tau^{-})$ and $f(t) = 1 - A\exp(-t/\tau^{+})$, respectively. The first intermediate state, S_{21}, decays with a time constant of τ_{21}^{-} = 66.3 ± 0.3 fs followed by the growth of the second intermediate state, S_{10}, with a timescale of τ_{10}^{+} = 83 ± 3 fs (τ_{10}^{+} has been computed by fitting $t \leq 200$ fs) consistent with a sequential down-hill "waterfall" mechanism. After reaching the maximum population, S_{10} decays with a time constant of τ_{10}^{-} = 262 ± 2 fs (for $t > 200$ fs) while the rise of S_1 occurs on a time scale of τ_{1}^{+} = 276 ± 1 fs implying ultrafast relaxation across S_{10}–S_1 state sequence. A more detailed view of the population flow is revealed in the probability density of the current state, depicted in the contour plot in Fig. 2(b). This picture already suggests that the relaxation mechanisms across dense states and from long-lived intermediates may be substantially different. It can be clearly seen that the relaxation process to S_1 is characterized by transient exciton trappings on S_{21} and S_{10} followed by an ultrafast funnel cascade through states in between.

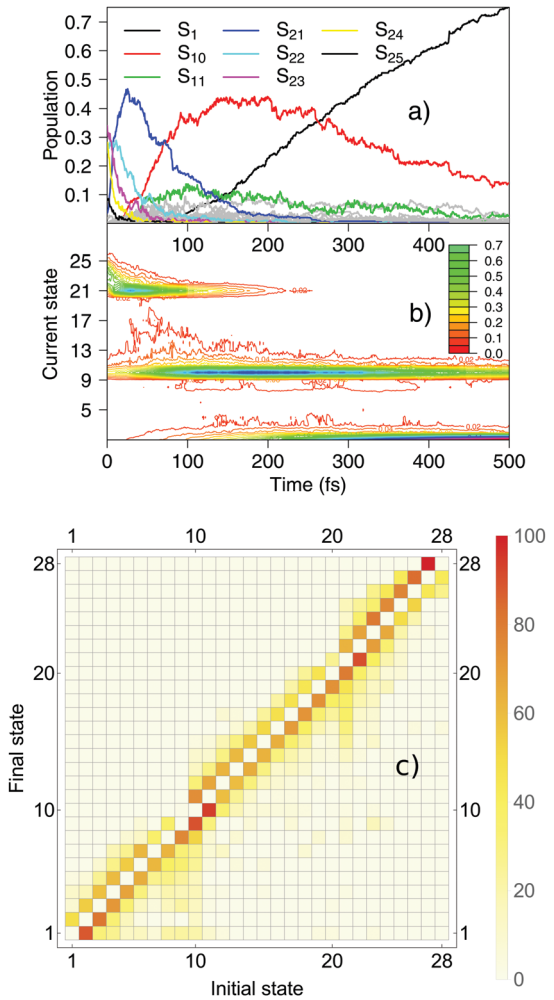

Fig. 2 (a) Evolution of electronic state populations during relaxation from the initial excitation S_{22}–S_{25} to the lowest energy state S_1. (b) Contour plot of the probability density of the current electronic state. (c) Percent of hops from each initial state to all possible final states. First off-diagonal represents sequential mechanism hopping between nearest neighbor states closest in energy. All other off-diagonals correspond to hops between states that are not closest in energy.

The number of hops between states can provide useful insights into the relaxation pathway by giving an indication of the non-adiabatic coupling strengths pairing states at different energy. Fig. 2(c) shows the percent of hops from the current (initial) state, i, to each final state, j, integrated across all trajectories. Specifically, the percent of hops is calculated as $\%\text{hops}_{i\to j} = \left(\text{hops}_{i\to j} \Big/ \sum_k \text{hops}_{i\to k}\right) \times 100$ where k represents all states. The plot includes all FSSH allowed hops, meaning that $S_i \rightleftarrows S_j$ transitions include potential subsequent backwards transitions. It is important to note that the percent of hops is not normalized allowing a large percent to be obtained even for events that are relatively rare. Here, the nearest-neighbour off-diagonal elements represent the $S_i \rightleftarrows S_{i\pm1}$ transitions corresponding to the sequential mechanism of hopping between states closest in energy. The other off-diagonals indicate hops between non-neighboring states. The plot suggests that during the relaxation from S_{28} to S_{21} and S_{20} to S_{10}, each intermediate state is populated in an approximately sequential fashion such as $S_i \to S_{i-1}$ where $28 > i > 21$ and $20 > i > 10$. However, the relaxation from S_{21} and S_{10} to lower energy excited states occurs differently. In that case, the higher energy electronic state is directly coupled to multiple lower energy states allowing for multichannel non-sequential electronic relaxation. For example, in the case of S_{21}, due to the large energy gap, the electronic state is coupled not only with energetically neighboring states S_{20} and S_{22}, but also with the range of states S_{19}–S_{15}. For S_{10}, where the downhill energy gap is the largest, the electronic population is transferred to the range of states S_9–S_1. In fact, Fig. 2(c) indicates that for all states below S_{10}, the sequential mechanism breaks down and transitions to all lower energy states emerge.

Next, to rationalize the spatial evolution of the electronic wave functions during internal conversion, we analyze the localization of the electronic transition density within each pyrene unit of the [4]CPY ring. For each state, the excited state distribution of participation number (calculated using eqn (2)) is constructed by collecting excited state geometries during NA-ESMD dynamics at all times for which the electronic state of interest defines the nuclear propagation. The excited state distribution of participation number by state is

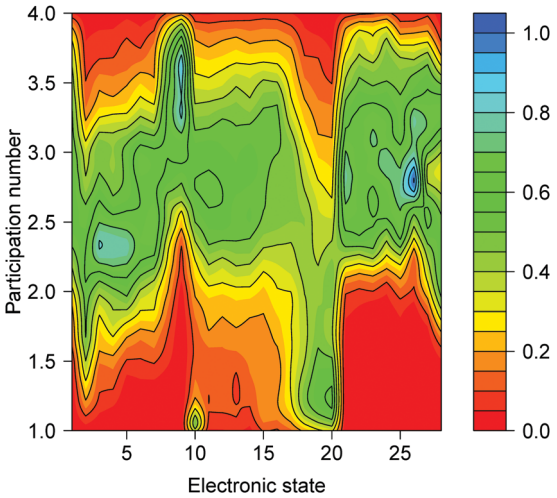

Fig. 3 Contour plot of the probability density of participation number during excited state dynamics for each state where each of the four pyrene monomers is considered.

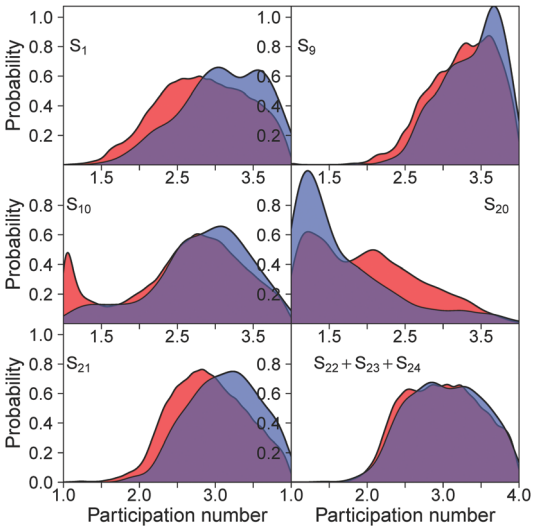

Fig. 4 Distribution of participation number for relevant states at the initial time t = 0 (blue) and during excited state dynamics (red).

presented in Fig. 3. The contour plot reveals sudden changes in localization involving the long-lived states S_{21} and S_{10} with respect to their neighbors S_{20} and S_9, respectively. In contrast with all the other states, where the electronic transition density is primarily delocalized over 2–4 pyrene units, S_{10} and S_{20} are essentially confined to a single monomer. This abrupt change in localization reduces the overlap, and thus the non-adiabatic coupling, with the state directly below or above in energy. The overlap between neighboring states can be quantified as the common area between the excited state participation number distributions, as presented in Table 1. Indeed, the overlap between states S_{20}/S_{21} is 0.43 and S_9/S_{10} is 0.61, being considerably smaller than for the remaining states where S_i/S_{i-1} has an average value of 0.88.

It is well known that the redistribution of excitation energy during dynamics can cause changes in (de)localization. Therefore, it is interesting to compare the initial ground state distribution of participation number to the excited state distribution during dynamics for relevant states. The initial distributions are made using equilibrated ground state structures at time t = 0 and the excited state distributions are evaluated using all times throughout NA-ESMD simulations for which the relevant state defines the current state, that is, the state that dictates the nuclear motion according to the FSSH approach. In this way, we can evaluate the impact of specific excited state gradients on the electronic transition density localization for a given state, and compare them with the corresponding values dictated by ground state gradients. Fig. 4 displays a few relevant comparisons of the ground state and excited state participation number distributions. The ground state distribution of participation number (blue curve) and the average value during the excited state dynamics (red curve) are plotted together to show how the initial (de)localization of the electronic transition density changes due to dynamics on the excited state surface. In the case of S_{10}, the initial ground state distribution has a maximum at PN = 3 corresponding delocalization, whereas the excited state distribution changes to a bimodal structure with maxima at PN = 1.1 and 2.7, indicating an increased probability of localization (PN = 1.1) during dynamics. The dynamics have an opposite effect on the localization of S_{20} where the well localized transition density with a maximum probability of PN = 1.2 becomes more delocalized with a maximum probability of PN = 2.1. Meanwhile, the transition density of S_{21} experiences relatively little change and remains delocalized with maxima PN = 3.2 at t = 0 and an average of PN = 2.8 during dynamics, similar to the behavior observed in S_9. The mismatch in localization between the neighboring states S_{10} and S_9 as well as S_{21} and S_{20} persists during dynamics, giving rise to the poor overlap and low non-adiabatic couplings. In contrast, the range of states S_{22}–S_{24} have similar localization to S_{21} allowing good overlap.

The sudden changes in localization associated with the long-lived states (Fig. 3) and the reduced overlap with neighboring states during the excited state dynamics (Fig. 4) both indicate the sensitivity of S_{21} and S_{10} to excited state gradients which significantly impact their electronic wavefunctions and non-adiabatic couplings with other states. The direction of the non-adiabatic

Table 1 Overlap of excited state participation number distributions between states S_i and S_{i-1}

States	Overlap	States	Overlap
S_2/S_1	0.65	S_{16}/S_{15}	0.95
S_3/S_2	0.81	S_{17}/S_{16}	0.89
S_4/S_3	0.95	S_{18}/S_{17}	0.83
S_5/S_4	0.94	S_{19}/S_{18}	0.87
S_6/S_5	0.91	S_{20}/S_{19}	0.93
S_7/S_6	0.96	**S_{21}/S_{20}**	**0.43**
S_8/S_7	0.75	S_{22}/S_{21}	0.93
S_9/S_8	0.80	S_{23}/S_{22}	0.96
S_{10}/S_9	**0.61**	S_{24}/S_{23}	0.93
S_{11}/S_{10}	0.90	S_{25}/S_{24}	0.90
S_{12}/S_{11}	0.97	S_{26}/S_{25}	0.85
S_{13}/S_{12}	0.96	S_{27}/S_{26}	0.80
S_{14}/S_{13}	0.97	S_{28}/S_{27}	0.83
S_{15}/S_{14}	0.93		

coupling vector can be interpreted as the main driving force on the nuclei during electronic transitions involving active phonons on both states.

4 Conclusion

Understanding the nonradiative relaxation mechanisms governed by the electron–phonon coupling is essential for many potential technologies based on π-conjugated materials. In this respect, atomistic dynamical simulations beyond the Born–Oppenheimer regime provide intricate details of the underlying photophysics. Here, we model the nonradiative relaxation processes in the circular pyrene tetramer [4]CPY. Ultrafast sequential quantum transitions across a dense manifold of excited states is the dominating mechanism of internal conversion owing to strong non-adiabatic couplings. Additionally, we observe the presence of two long-lived excited states, separated from lower energy states by large energy gaps, which create phonon bottlenecks in the electronic relaxation. Analysis of adiabatic state populations confirms that the overall internal conversion timescale ($\sim$276 fs) can be attributed to the intermediate bottleneck states with lifetimes extending to $\sim$262 fs.

Within the considered energy range ($\sim$280–400 nm), the majority of excited states in [4]CPY are delocalized across multiple pyrene units. However, there are localized excitations on a single pyrene, which are associated with the long-lived states. The mismatch in localization decreases the overlap with neighboring states, which along with the large energy gap, substantially reduces the non-adiabatic couplings controlling the efficiency of quantum transitions. This causes an interruption in the sequential transition order and enables multichannel relaxation. Accumulation of energy on states S_{21} and S_{10} follow different relaxation pathways involving direct hops from these states to different states in the range of S_{19}–S_{15} and S_9–S_1, respectively. These multiple pathways constitute a large number of options for energy relaxation to the final lowest energy S_1 state that directly depend on transient relative couplings between states. This feature is difficult to analyze statistically due to the large combination of possible hopping sequences, however, our analysis verifies the interruption of the sequential mechanism during the energy relaxation from the bottleneck states. Thus, our simulations exemplify a delicate interplay between sequential and multichannel scenarios of nonradiative relaxation. The former ensures ultrafast quantum transitions between quasi-degenerate coupled excited states with similar wavefunction delocalization. In contrast, the latter dominates in cases where the electronic excitations have substantially different spatial delocalization and are separated by large energy gaps.

Such long-lived electronic states have been reported in the photophysics of many nano-structured materials.[58–63] Here, large gaps between electronic bands necessitate vibronic relaxation *via* multi-phonon and off-resonant processes, thus slowing the electronic relaxation, an effect commonly known as phonon bottleneck.[64] Subsequently, other ultrafast electronic processes may dominate. For example, dissociation of the exciton into charges occurs on the $\sim$100 fs timescale in bulk-heterojunction organic solar cells,[65] which involves hot carrier formation.[66] Similar timescales have been reported for singlet fission.[67] Electron injection in dye-TiO_2[68] and quantum dot-TiO_2[69] systems may happen under 50 fs. Thus, control of electronic relaxation on the molecular level can lead to excited states which can be considered ''long-lived'' with a lifetime of hundreds of femtoseconds allowing the common nonradiative relaxation to be superseded by much faster processes, enabling for example, hot-carrier extraction in light-harvesting applications.[70]

Acknowledgements

R. F. M. and S. F. A. are supported by CONICET, UNQ, ANPCyT (PICT-2014-2662). S. T. and T. N. acknowledge support from Los Alamos National Laboratory (LANL) Directed Research and Development Funds. Los Alamos National Laboratory is operated by Los Alamos National Security, LLC, for the National Nuclear Security Administration of the U.S. Department of Energy under contract DE-AC52-06NA25396. We acknowledge support of the Center for Nonlinear Studies (CNLS), the Center for Integrated Nanotechnology (CINT), a U.S. Department of Energy, Office of Basic Energy Sciences user facility, and the LANL Institutional Computing (IC) Program for providing computational resources.

References

1 Z. Chen, D. Jiang, X. Lu, H. F. Bettinger, S. Dai, P. V. R. Schleyer and K. N. Houk, *Org. Lett.*, 2007, **9**, 5449–5452.
2 R. Jasti, J. Bhattacharjee, J. B. Neaton and C. R. Bertozzi, *J. Am. Chem. Soc.*, 2008, **130**, 17646–17647.
3 S. C. Kornmayer, B. Esser and R. Gleiter, *Org. Lett.*, 2009, **11**, 725–728.
4 E. S. Hirst, F. Wang and R. Jasti, *Org. Lett.*, 2011, **13**, 6220–6223.
5 Y. Segawa, A. Yagi, H. Ito and K. Itami, *Org. Lett.*, 2016, **18**, 1430–1433.
6 E. Heilbronner, *Helv. Chim. Acta*, 1954, **37**, 921–935.
7 T. Kawase and H. Kurata, *Chem. Rev.*, 2006, **106**, 5250–5273.
8 K. Tahara and Y. Tobe, *Chem. Rev.*, 2006, **106**, 5274–5290.
9 B. D. Steinberg and L. T. Scott, *Angew. Chem., Int. Ed.*, 2009, **48**, 5400–5402.
10 R. Gleiter, B. Esser and S. C. Kornmayer, *Acc. Chem. Res.*, 2009, **42**, 1108–1116.
11 D. Eisenberg, R. Shenhar and M. Rabinovitz, *Chem. Soc. Rev.*, 2010, **39**, 2879–2890.
12 A. Yagi, Y. Segawa and K. Itami, *J. Am. Chem. Soc.*, 2012, **134**, 2962–2965.
13 H. Omachi, T. Nakayama, E. Takahashi, Y. Segawa and K. Itami, *Nat. Chem.*, 2013, **5**, 572–576.
14 B. L. Merner, L. N. Dawe and G. J. Bodwell, *Angew. Chem.*, 2009, **121**, 5595–5599.
15 J. Q. Gong, P. Parkinson, D. V. Kondratuk, G. Gil-Ramirez, H. L. Anderson and L. M. Herz, *J. Phys. Chem. C*, 2015, **119**, 6414–6420.

16 B. M. Wong, *J. Phys. Chem. C*, 2009, **113**, 21921–21927.
17 H. M. Jaeger, K. Hyeon-Deuk and O. V. Prezhdo, *Acc. Chem. Res.*, 2013, **46**, 1280–1289.
18 Y. Segawa, A. Fukazawa, S. Matsuura, H. Omachi, S. Yamaguchi, S. Irle and K. Itami, *Org. Biomol. Chem.*, 2012, **10**, 5979–5984.
19 L. Adamska, I. Nayyar, H. Chen, A. K. Swan, N. Oldani, S. Fernandez-Alberti, M. R. Golder, R. Jasti, S. K. Doorn and S. Tretiak, *Nano Lett.*, 2014, **14**, 6539–6546.
20 S. E. Lewis, *Chem. Soc. Rev.*, 2015, **44**, 2221–2304.
21 A. Yagi, G. Venkataramana, Y. Segawa and K. Itami, *Chem. Commun.*, 2014, **50**, 957–959.
22 T. Iwamoto, E. Kayahara, N. Yasuda, T. Suzuki and S. Yamago, *Angew. Chem., Int. Ed.*, 2014, **53**, 6430–6434.
23 A. Laurent, *Ann. Chim. Phys.*, 1837, **66**, 136.
24 T. M. Figueira-Duarte and K. Müllen, *Chem. Rev.*, 2011, **111**, 7260–7314.
25 F. M. Winnik, *Chem. Rev.*, 1993, **93**, 587–614.
26 K. Kalyanasundaram and J. K. Thomas, *J. Am. Chem. Soc.*, 1977, **99**, 2039–2044.
27 J.-S. Yang, C.-S. Lin and C.-Y. Hwang, *Org. Lett.*, 2001, **3**, 889–892.
28 J. Huang, Y. Wu, Y. Chen, Z. Zhu, X. Yang, C. J. Yang, K. Wang and W. Tan, *Angew. Chem., Int. Ed.*, 2011, **50**, 401–404.
29 S. K. Kim, J. H. Bok, R. A. Bartsch, J. Y. Lee and J. S. Kim, *Org. Lett.*, 2005, **7**, 4839–4842.
30 P. Somerharju, *Chem. Phys. Lipids*, 2002, **116**, 57–74.
31 J. Strauss and J. Daub, *Org. Lett.*, 2002, **4**, 683–686.
32 Y. Suzuki, T. Morozumi, H. Nakamura, M. Shimomura, T. Hayashita and R. A. Bartsh, *J. Phys. Chem. B*, 1998, **102**, 7910–7917.
33 C. Monahan, *Chem. Commun.*, 1998, 431–432.
34 S. Diring, F. Camerel, B. Donnio, T. Dintzer, S. Toffanin, R. Capelli, M. Muccini and R. Ziessel, *J. Am. Chem. Soc.*, 2009, **131**, 18177–18185.
35 A. Thiessen, H. Wettach, K. Meerholz, F. Neese, S. Höger and D. Hertel, *Org. Electron.*, 2012, **13**, 71–83.
36 T. Nelson, S. Fernandez-Alberti, V. Chernyak, A. E. Roitberg and S. Tretiak, *J. Phys. Chem. B*, 2011, **115**, 5402–5414.
37 T. Nelson, S. Fernandez-Alberti, V. Chernyak, A. Roitberg and S. Tretiak, *J. Chem. Phys.*, 2012, **136**, 054108.
38 S. Fernandez-Alberti, A. Roitberg, T. Nelson and S. Tretiak, *J. Chem. Phys.*, 2012, **137**, 014512.
39 T. Nelson, S. Fernandez-Alberti, A. E. Roitberg and S. Tretiak, *Chem. Phys. Lett.*, 2013, **590**, 208–213.
40 T. Nelson, S. Fernandez-Alberti, A. E. Roitberg and S. Tretaik, *J. Chem. Phys.*, 2013, **138**, 224111.
41 T. Nelson, S. Fernandez-Alberti, A. E. Roitberg and S. Tretaik, *Acc. Chem. Res.*, 2014, **47**, 1155–1164.
42 J. Tully, *J. Chem. Phys.*, 1990, **93**, 1061–1071.
43 M. Paterlini and D. Ferguson, *Chem. Phys.*, 1998, **236**, 243–252.
44 P. Attard, *J. Chem. Phys.*, 2009, **130**, 194113.
45 S. Tretiak, C. Isborn, A. Niklasson and M. Challacombe, *J. Chem. Phys.*, 2009, **130**, 054111.
46 S. Tretiak, V. Chernyak and S. Mukamel, *J. Chem. Phys.*, 1996, **105**, 8914–8928.
47 F. Furche and R. Ahlrichs, *J. Chem. Phys.*, 2002, **117**, 7433–7447.
48 R. Send and F. Furche, *J. Chem. Phys.*, 2010, **132**, 044107.
49 I. Tavernelli, B. F. E. Curchod, A. Laktionov and U. Rothlisberger, *J. Chem. Phys.*, 2010, **133**, 194104.
50 S. Tretiak, V. Chernyak and S. Mukamel, *J. Am. Chem. Soc.*, 1997, **119**, 11408–11419.
51 S. Tretiak, V. Chernyak and S. Mukamel, *Chem. Phys. Lett.*, 1996, **259**, 55–61.
52 D. J. Thouless, *The Quantum Mechanics Of Many-Body Systems*, Academic Press, New York, 1972.
53 E. R. Davidson, *Reduced Density Matrices in Quantum Chemistry*, Academic Press, New York, 1976.
54 M. J. S. Dewar, E. G. Zoebisch, E. F. Healy and J. J. P. Stewart, *J. Am. Chem. Soc.*, 1985, **107**, 3902–3909.
55 C. Wu, S. V. Malinin, S. Tretiak and V. Y. Chernyak, *Phys. Rev. Lett.*, 2008, **100**, 057405.
56 S. Tretiak and S. Mukamel, *Chem. Rev.*, 2002, **102**, 3171.
57 D. Ondarse-Alvarez, N. Oldani, S. Tretiak and S. Fernandez-Alberti, *J. Phys. Chem. A*, 2014, **118**, 10742–10753.
58 S. V. Kilina, D. S. Kilin and O. V. Prezhdo, *ACS Nano*, 2009, **3**, 93–99.
59 O. Prezhdo, *Chem. Phys. Lett.*, 2008, **460**, 1–9.
60 Y. Yang, D. P. Ostrowski, R. M. France, K. Zhu, J. van de Lagemaat, J. M. Luther and M. C. Beard, *Nat. Photonics*, 2016, **10**, 53–59.
61 S. Huang and D. S. Kilin, *J. Chem. Theory Comput.*, 2014, **10**, 3996–4005.
62 J. P. Trinastic, I.-H. Chu and H.-P. Cheng, *J. Phys. Chem. C*, 2015, **119**, 22357–22369.
63 C. Burda, X. Chen, R. Narayanan and M. A. El-Sayed, *Chem. Rev.*, 2005, **105**, 1025–1102.
64 A. Pandey and P. Guyot-Sionnest, *Science*, 2008, **322**, 929–932.
65 L. G. Kaake, C. Zhong, J. A. Love, I. Nagao, G. C. Bazan, T.-Q. Nguyen, F. Huang, Y. Cao, D. Moses and A. J. Heeger, *J. Phys. Chem. Lett.*, 2014, **5**, 2000–2006.
66 A. E. Jailaubekov, A. P. Willard, J. R. Tritsch, W.-L. Chan, N. Sai, R. Gearba, L. G. Kaake, K. J. Williams, K. Leung, P. J. Rossky and X.-Y. Zhu, *Nat. Mater.*, 2013, **12**, 66–73.
67 W.-L. Chan, M. Ligges, A. Jailaubekov, L. Kaake, L. Miaja-Avila and X.-Y. Zhu, *Science*, 2011, **334**, 1541–1545.
68 W. R. Duncan and O. V. Prezhdo, *Annu. Rev. Phys. Chem.*, 2007, **58**, 143–184.
69 W. A. Tisdale, K. J. Williams, B. A. Timp, D. J. Norris, E. S. Aydil and X.-Y. Zhu, *Science*, 2010, **328**, 1543–1547.
70 R. T. Ross and A. J. Nozik, *J. Appl. Phys.*, 1982, **53**, 3813–3818.

